SCIENCE CHINA
Chemistry

•ARTICLES•

https://doi.org/10.1007/s11426-022-1479-x

Tandem organic solar cells with efficiency over 19% *via* the careful subcell design and optimization

Lingxian Meng[1†], Huazhe Liang[1†], Guangkun Song[1†], Mingpeng Li[1†], Yuzhong Huang[1], Changzun Jiang[1], Kai Zhang[2], Fei Huang[2], Zhaoyang Yao[1], Chenxi Li[1], Xiangjian Wan[1*] & Yongsheng Chen[1*]

[1]*State Key Laboratory and Institute of Elemento-Organic Chemistry, Centre of Nanoscale Science and Technology and Key Laboratory of Functional Polymer Materials, College of Chemistry, Nankai University, Tianjin 300071, China;*
[2]*State Key Laboratory of Luminescent Materials and Devices, South China University of Technology, Guangzhou 510640, China*

Received October 24, 2022; accepted December 2, 2022; published online January 16, 2023

The series-connected tandem device strategy is an effective approach to promote the efficiency of organic solar cells (OSCs) with broadened absorption range and alleviated thermalization and transmission loss. In this article, two nonfullerene acceptors, FBr-ThCl and BTP-4Se, with complementary absorptions covering the range from 300 to 1,000 nm were designed and synthesized for the front and rear cell, respectively. The front cell based on D18:FBr-ThCl exhibited a V_{oc} of 1.053 V with high external quantum efficiency (EQE) response values ranging from 300 to 740 nm. The rear cell with a ternary active layer PM6:BTP-4Se:F-2F was optimized and afforded the V_{oc} of 0.840 V and J_{sc} of 26.88 mA cm^{-2}. Subsequently, the tandem device was constructed with a fully solution-processed interconnected layer of ZnO/PEDOT:PSS/PMA, and demonstrated a power conversion efficiency (PCE) of 19.55% with a V_{oc} of 1.880 V, a J_{sc} of 13.25 mA cm^{-2} and an *FF* of 78.47%.

tandem device, organic solar cells, front cell, rear cell, power conversion efficiency

Citation: Meng L, Liang H, Song G, Li M, Huang Y, Jiang C, Zhang K, Huang F, Yao Z, Li C, Wan X, Chen Y. Tandem organic solar cells with efficiency over 19% *via* the careful subcell design and optimization. *Sci China Chem*, 2023, 66, https://doi.org/10.1007/s11426-022-1479-x

1 Introduction

Organic solar cell (OSC) is thought as one promising choice for next generation green technologies due to the merits of low-cost, solution-process and flexibility [1–5]. In the past decade, great progress has been witnessed for OSCs. The power conversion efficiencies (PCEs) of single-junction OSCs have reached over 18% through the innovative materials design and device optimization [6–11]. However, the performance of OSCs still lags behind other photovoltaic technologies and there are various restrictions for further improvement of the single junction OSCs. The intrinsic low charge mobilities of organic materials and the inherent narrow absorption windows of organic semiconductors are detrimental for achieving the high photocurrent [12,13]. Besides, single-junction OSCs inevitably suffer from the thermalization loss and transmission loss [14]. To address the above issues, one promising strategy is to develop tandem devices by employing two or more subcells with complementary absorptions connected together. In addition, the tandem OSCs can maximize the privileges of organic materials, *i.e.*, the high diversity and easily tunable absorptions and energy levels [12,15–20]. To obtain high performance series-connected tandem OSCs, it is required to have the subcells with low energy loss (E_{loss}) as well as efficient and complementary absorptions. In the past decades, great efforts have been devoted to the dedicated design and screening of

†These authors contributed equally to this work.
*Corresponding authors (email: xjwan@nankai.edu.cn; yschen99@nankai.edu.cn)

subcell materials to meet the requirement of tandem OSCs [12,14,21–28]. Thanks to the rapid development of non-fullerene acceptors, especially the acceptor-donor-acceptor (A-D-A) type acceptors which have easily tunable band structures, absorptions and low E_{loss} [5,13,29–33], great opportunities have emerged for the subcell materials design in constructing high-efficiency tandem OSCs. In 2018, we proposed a semi-empirical analysis model, which can direct the subcells materials design and screening and effectively predict the efficiencies of tandem OSCs [12]. Under the guidance of the analysis, two A-D-A type acceptors F-M and O6T-4F with complementary absorptions were screened and selected for the front and rear subcells. After device optimization, an outstanding PCE of 17.36% was achieved [12]. According to the analysis, PCE over 25% could be attained for the tandem OSCs *via* the careful subcell materials design and screening. It is worth noting that the V_{oc} and J_{sc} are always two entangled parameters for the state-of-the-art single junction devices and there are no subcells could concurrently meet all the ideal requirements for tandem OSCs. Therefore, in our following work, we have proposed the strategy of subtle tradeoff for V_{oc} and J_{sc} to fabricate high-efficiency tandem OSCs, and a tandem OSC with a promising PCE of 14.52% was fabricated by using two subcells incorporating the same polymer donor PBDB-T and two acceptors F-M and NNBDT with the complementary absorptions [25]. Just recently, using the similar strategy, we have constructed a tandem OSC and achieved a PCE of 18.67% *via* the careful materials design and selection of two subcells with the D18:F-ThBr and PM6:CH1007:$PC_{71}BM$ with complementary absorption [34]. In fact, the above strategy has also been used in the community for constructing tandem OSCs and exciting PCEs of 19%–20% have been achieved recently [15,35,36].

With above analysis and combined with the guidance of our semi-empirical analysis, in this article, we designed and synthesized two nonfullerene acceptors to fabricate the high-effiency tandem device. Firstly, we designed an acceptor FBr-ThCl by introducing the electron-withdrawing bromine atom on the backbone and the weaken electron-withdrawing chlorinated thiophene-fused end group based on F-M, one efficient acceptor used in front cell we previously reported [12], to enlarge its band gap and enhance its packing ability to obtain high V_{oc} and *FF*. The device of D18:FBr-ThCl exhibited a PCE of 12.72% with a high V_{oc} of 1.053 V, a J_{sc} of 15.33 mA cm^{-2} and a notable *FF* of 78.81%, highlighting the potential for the front cell. Secondly, considering the small E_{loss} and near infrared absorption of the Y6 derivatives based devices [29,37–39], we designed an acceptor BTP-4Se by introducing four selenium atoms on the Y6 backbone for the rear cell material, which shows an onset absorption around 1,000 nm with an optical bandgap of 1.26 eV. A ternary device based on PM6:BTP-4Se:F-2F was fabricated and gave a PCE of 16.56% with a high V_{oc} of 0.840 V, a J_{sc} of 26.88 mA cm^{-2}, and an *FF* of 73.36%. The infrared absorption together with its excellent photovoltaic parameters ensure PM6:BTP-4Se:F-2F a good option as rear cell. Finally, a tandem cell with D18:FBr-ThCl as the front cell and PM6:BTP-4Se:F-2F as rear cell was fabricated by using a fully solution-processed interconnected layer (ICL) of ZnO/PEDOT:PSS/PMA and achieved an outstanding PCE of 19.55% with a V_{oc} of 1.880 V, a J_{sc} of 13.25 mA cm^{-2} and a notable *FF* of 78.47%.

2 Results and discussion

2.1 Front cell design and photovoltaic property

In the tandem OSCs, front cells always play the same important role compared with rear cells. However, compared with the wide study on rear cells, less attention has been focused on the front cells. In fact, to date, it is still a challenge to design suitable front cells for fabricating high-efficiency tandem OSCs. Firstly, according to the semi-empirical model, the ideal front cells should have an absorption onset around 720 nm with the band gap of 1.72 eV and as low as E_{loss}. The band gap of the active layer is determined by the components with the smallest optical energy gap. For the state-of-the-art OSCs, acceptors always have the lower band gap than that of the donors, and thus determine the bandgap of the corresponding blend active layer. Presently, most of the wide bandgap nonfullerene acceptors based devices suffer from the high E_{loss}. Thus, it is necessary to design acceptors with wide bandgap and low E_{loss} for constructing high-efficiency tandem OSCs. Secondly, the front cells should have efficient external quantum efficiency (EQE) response to ensure the high J_{sc} in the tandem cells. Meanwhile, high *FF* is also required for the front cells to get the overall *FF* value of the tandem OSCs. Lastly, the front cells have to be strong enough to ensure the subsequent spin coating and thermal treatments of the ICL and rear cells. Owing to the above critical requirement for front cells, although nonfullerene acceptors, especially A-D-A type acceptors, have given more opportunities on materials design for single and tandem OSCs, only a few effective front cells have been reported to date. That is why only P3HT:PCBM has been widely used as front cell to construct tandem OSCs in the fullerene era of OSCs. With above consideration in mind, herein, we designed an acceptor FBr-ThCl based on the acceptor F-M in our previous work of tandem OSCs. The chemical structure of FBr-ThCl is shown in Figure 1a and its synthetic route and the detailed characterization data are provided in the Supporting Information online. Figure 1b depicted the UV-vis absorption of the acceptor in solution and film state, which exhibits a maximum absorption peak at 636 nm in solution state and 665 nm in film state with an

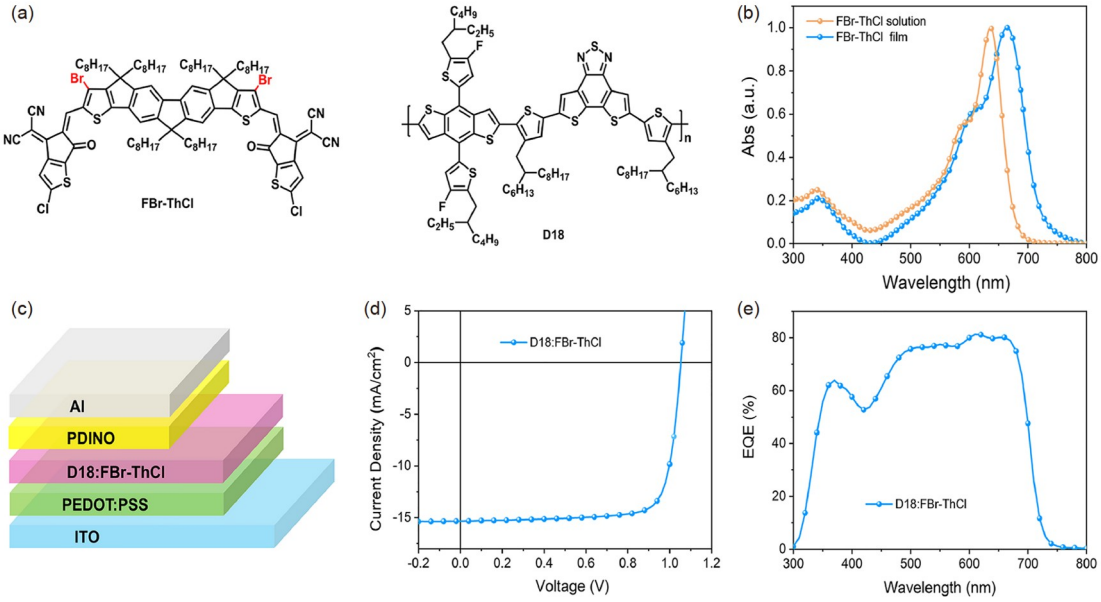

Figure 1 (a) Chemical structures of the small molecule acceptor FBr-ThCl and donor D18. (b) Normalized UV-vis absorption spectra of FBr-ThCl in solution and neat film state. (c) The device architecture of the conventional OSCs. (d) *J*-*V* curves and (e) EQE curves of the optimized device based on D18:FBr-ThCl (color online).

absorption onset of 738 nm and the corresponding optical bandgap of 1.68 eV. From the cyclic voltammetry (CV) curves (Figure S1, Supporting Information online), the highest occupied molecular orbital (HOMO) and lowest unoccupied molecular orbital (LUMO) energy levels of FBr-ThCl was estimated to be −5.84 and −3.78 eV, respectively. Compared with F-M, the FBr-ThCl shows a larger bandgap and more suitable for the front cell.

To investigate the photovoltaic performance of the acceptor, the single junction cell was fabricated using a normal device structure of indium tin oxide (ITO)/PEDOT:PSS/active layer/PDINO/Al (Figure 1c). For complementary absorption and matched energy level, D18 was selected as the donor material. After systematically optimization, the optimal D18:FBr-ThCl device shows a PCE of 12.72% with a V_{oc} of 1.053 V, a J_{sc} of 15.33 mA cm^{-2} and an excellent *FF* of 78.81%. The photovoltaic parameters are listed in Table 1 and the current density-voltage (*J*-*V*) characteristic curve of the optimal device is depicted in Figure 2d. Figure 2e shows the EQE curves of the optimal device, which displays a high EQE response in the range from 300 to 740 nm with an integral current density of 15.26 mA cm^{-2}. The high V_{oc}, J_{sc} together with the outstanding *FF*, suggesting that D18:FBr-ThCl should be a good option as the front cell in the tandem device.

The transient photovoltage and photocurrent (TPV and TPC) measurements are carried out to investigate the charge carrier dynamics of the devices. As shown in Figure S2, the D18:FBr-ThCl device shows a short sweepout time of 0.38 μs and a longer carrier lifetime of 23.2 μs, indicating that the device could effectively facilitate charge carrier extraction and show weaker recombination. The space-charge-limited current (SCLC) method was also employed to gain more insight of the properties of carrier transport as shown in Figure S3. The electron and hole mobilities were calculated to be 3.47 × 10^{-4} and 3.17 × 10^{-4} cm^2 V^{-1} s^{-1}, respectively, and with the μ_e/μ_h value of 1.09. The high mobility and balanced μ_e/μ_h in the blend film of D18:FBr-ThCl contribute to suppress the charge accumulation and recombination and favor the charge transport, thus support the high *FF* of the device.

The surface morphology of the D18:FBr-ThCl was studied by the atomic force microscopy (AFM). As shown in Figure 2a, b, the blend film shows smooth surface morphology with the root-mean-square roughness (R_q) value of 1.17 nm. And clear nanofibers can be observed in the phase images, which can benefit for the charge carriers generation, charge transport and thus the enhancement of the J_{sc} and *FF* [40]. Grazing incidence wide-angle X-ray scattering (GIWAXS) measurement was carried out to investigate the molecular packing motifs in the film. As depicted in Figure 2c–e, the pure film of FBr-ThCl and the blend film of D18:FBr-ThCl both show clear face-on packing with a strong π-π stacking diffraction peaks (010) in out-of-plane (OOP) direction and lamellar packing diffraction (100) in in-plane (IP) direction. For the pristine pure film, the FBr-ThCl exhibits a π-π stacking distance of 3.58 Å with a crystal coherence length (CCL) value of 66.42 Å. In contrast, in the D18:FBr-ThCl blend film, a larger π-π stacking distance of 3.64 Å and smaller CCL value of 44.76 Å was observed, indicating that

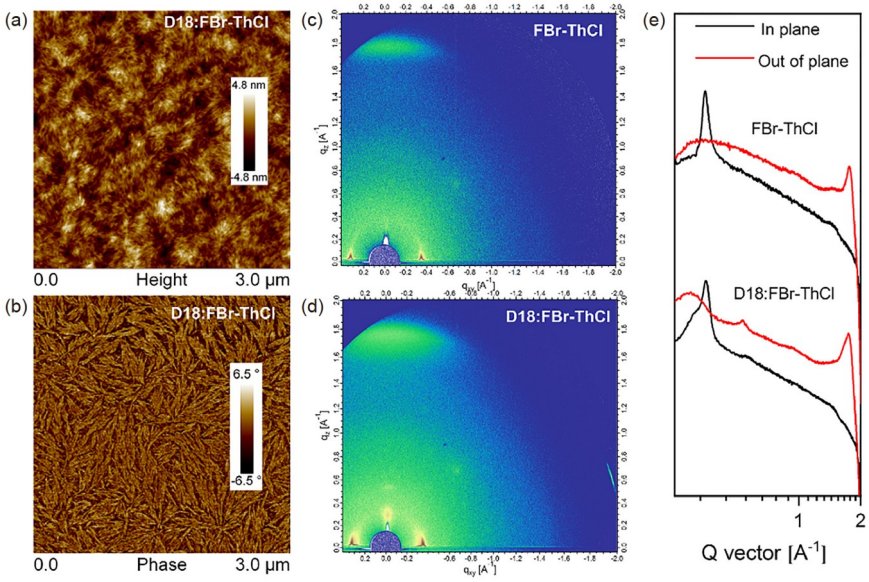

Figure 2 (a) AFM height image and (b) phase images of D18:FBr-ThCl blend. 2D-GIWAXD diffraction images of (c) the pure film of FBr-ThCl and (d) D18:FBr-ThCl blend. (e) 1D plots of the films in the in-plane and out-of-plane direction (color online).

Table 1 The optimized photovoltaic parameters of optimal single junction devices under the illumination of AM 1.5G (100 mW cm^{-2})

Active layer	V_{oc} (V)	*FF* (%)	J_{sc} (mA/cm^2)	PCE (%)
D18:FBr-ThCl	1.053	78.81	15.33	12.72 (12.54)
PM6: BTP-4Se:F-2F	0.840	73.36	26.88	16.56 (16.33)
Tandem device	1.880	78.47	13.25	19.55 (19.15)

a) The average values in parentheses are obtained from 10 independent cells.

the blend film could alleviate the over-aggregation, form proper phase separation, and facilitate charge transport in the device.

The E_{loss} of the device D18:FBr-ThCl was conducted according to the Shockley-Queisser (SQ) theory [41]. Based on the equation of $E_{loss} = E_{gap} - qV_{oc}=(E_g - qV_{oc,sq}) + (qV_{oc,sq} - q\Delta V_{oc,rad}) + (q\Delta V_{oc,rad}-qV_{oc})= \Delta E_1 + \Delta E_2 + \Delta E_3$, where the E_{gap} was estimated by the intersections between the absorption and emission spectra of the low bandgap component FBr-ThCl (Figure S4a). ΔE_1 is the radiative recombination loss above the bandgap, ΔE_2 is the radiative recombination loss below the bandgap, ΔE_3 is the nonradiative energy loss [42]. The total E_{loss} of the device D18:FBr-ThCl was 0.601 eV. For detailed energy loss as summarized in Table S1 (Supporting Information online), the device showed the ΔE_1 value of 0.269 eV, comparable with other typical OSCs. The third part ΔE_3, was calculated to be 0.304 eV from the EQE of electroluminescence (EQE_{EL}) following the equation of $\Delta E_3=-kT\ln(EQE_{EL})$ (Figure S4b), which is clearly the main reason for the energy loss of the device. The ΔE_2 with value of 0.028 eV was obtained from the above equation. According to the established results, ΔE_3 or the nonradiative loss can be decreased by enhancing the luminescent efficiency of the low band gap component in the active layers and reducing the energy offset between donor and acceptor [43]. It is believed that higher V_{oc} of front cell can be designed through the careful design of the acceptor and selection of the donor.

2.2 Rear cell design and photovoltaic property

In the past decade, for the fabrication of tandem OSCs, more attentions have been drawn on the design of rear cells with infrared absorptions. The target is to form complementary absorption with the front cells and ensure high J_{sc} of the tandem devices. However, the V_{oc} and *FF* of the rear cells have not received the same attentions as the infrared absorptions or J_{sc}. In fact, the three photovoltaic parameters should be concurrently considered according to the analysis model. With these, considering the infrared absorption and low E_{loss} of the devices based on Y6 and its derivatives, just recently, we have screened CH1007, a Y6 derivative with two selenium atoms substitution on the molecular backbone and infrared absorption as the rear cell acceptor to fabricate tandem OSC and achieved a PCE of 18.67% [34]. To further broaden the absorption range, herein, we design an acceptor named BTP-4Se by introducing four selenium atoms substitution on the Y6 backbone (Figure 3a) as the rear cell

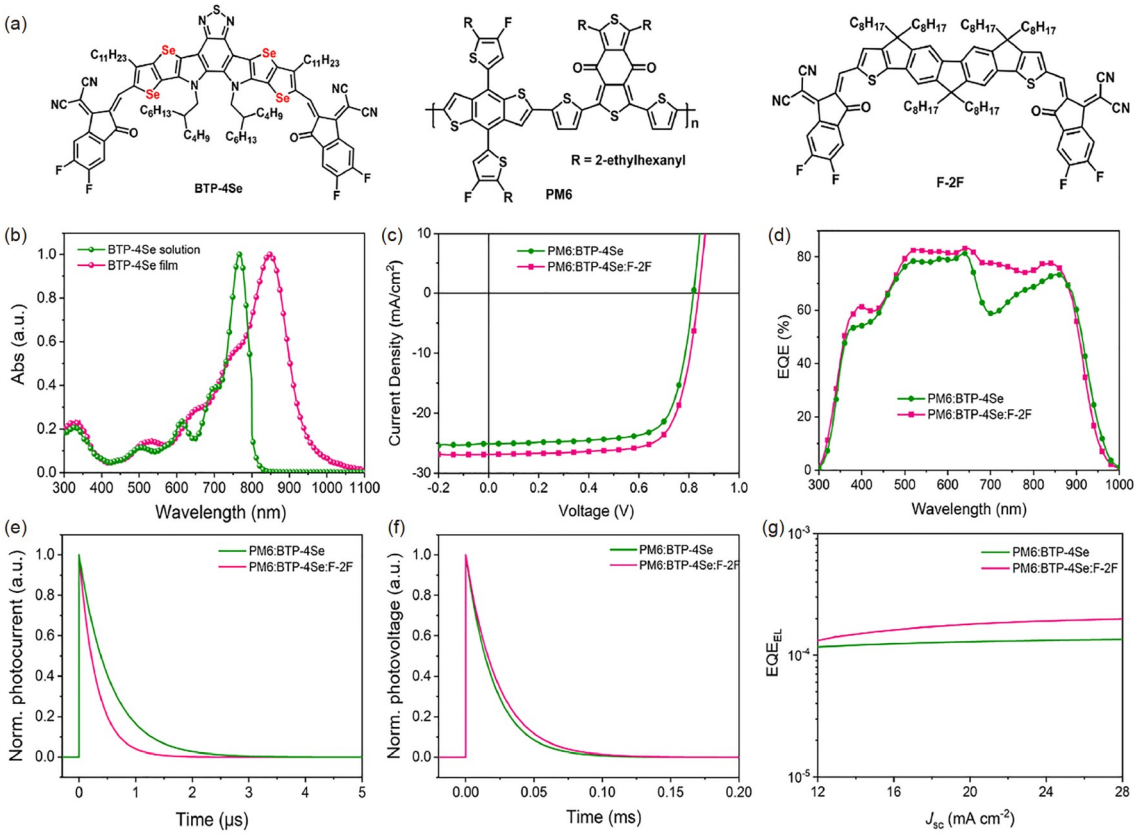

Figure 3 (a) Chemical structures of BTP-4Se, PM6 and F-2F. (b) Normalized UV-vis absorption spectra of BTP-4Se in solution and neat films state. (c) *J*-*V* curves and (d) EQE curves of the optimal OSCs based on PM6:BTP-4Se and PM6:BTP-4Se:F-2F. (e) Transient photocurrent measurements. (f) Transient photovoltage measurements and (g) EQE_{EL} curves of optimal PM6:BTP-4Se and PM6:BTP-4Se:F-2F-based devices (color online).

acceptor. The synthetic routes and detailed characterization data of BTP-4Se are provided in the Supporting Information online. The BTP-4Se film shows a maximum absorption peak at 847 nm with an absorption edge of 983 nm as shown in Figure 3b, which is clearly redshifted compared with Y6 and CH1007.

To evaluate the photovoltaic performance of BTP-4Se, the single junction device with the architecture of ITO/PEDOT:PSS/active layer/PDINO/Ag was fabricated. Considering the HOMO and LUMO values of the BTP-4Se (−5.62 and −3.88 eV) (Figure S5), PM6 was used as donor. The optimal device based on BTP-4Se delivered a PCE of 15.13% with a V_{oc} of 0.819 V, a J_{sc} of 25.11 mA cm^{-2} and an *FF* of 73.57%. Despite of the decent V_{oc} and *FF*, the J_{sc} of the PM6:BTP-4Se is not sufficient to construct efficient tandem OSCs. To further improve the performance, F-2F was added as the third component in the above binary system, which has a complementary absorption in the range of 600–800 nm with the PM6 and BTP-4Se [44]. With device optimization, the ternary device demonstrated a PCE of 16.56% with the nearly remained high *FF* of 73.36% and simultaneously improved V_{oc} of 0.840 V and J_{sc} of 26.88 mA cm^{-2}. The corresponding *J*-*V* curves are shown in Figure 3c. As depicted in Figure 3d, the ternary device exhibits an enhanced EQE response in the range of 600–850 nm, corresponding to a higher integrated photocurrent value of 26.15 mA cm^{-2} than that of the binary device with value of 24.40 mA cm^{-2}, which can be attributed to the improved light harvesting with complementary absorption and better morphology as discussed below, indicating the potential as the candidate for the rear cell in the tandem devices.

To illustrate the effect of the third component F-2F on charge transport behaviors, SCLC measurement was carried out as shown in Figure S6. The μ_e and μ_h of the ternary device are 4.19×10^{-4} and 4.05×10^{-4} cm^2 V^{-1} s^{-1} with μ_e/μ_h of 1.03, which is higher and more balanced than the binary device of 1.72×10^{-4} and 2.46×10^{-4} cm^2 V^{-1} s^{-1} for the μ_e and μ_h with a μ_e/μ_h of 0.70, suggesting the improved charge transport and higher J_{sc} in ternary blend. Furthermore, as shown in the TPC and TPV measurements (Figure 3e, f), the sweepout time of the binary and ternary blend is 0.56 and 0.31 μs and the carrier lifetime of the binary and ternary blend is 20.3 and 23.2 μs, respectively. The shorter sweepout time and longer carrier lifetime demonstrate the superior charge extraction and lower charge recombination loss in the ternary device.

Subsequently, the morphological differences between the binary and ternary blends were investigated by AFM. In the height images (Figure 4a, b), the binary and ternary blends

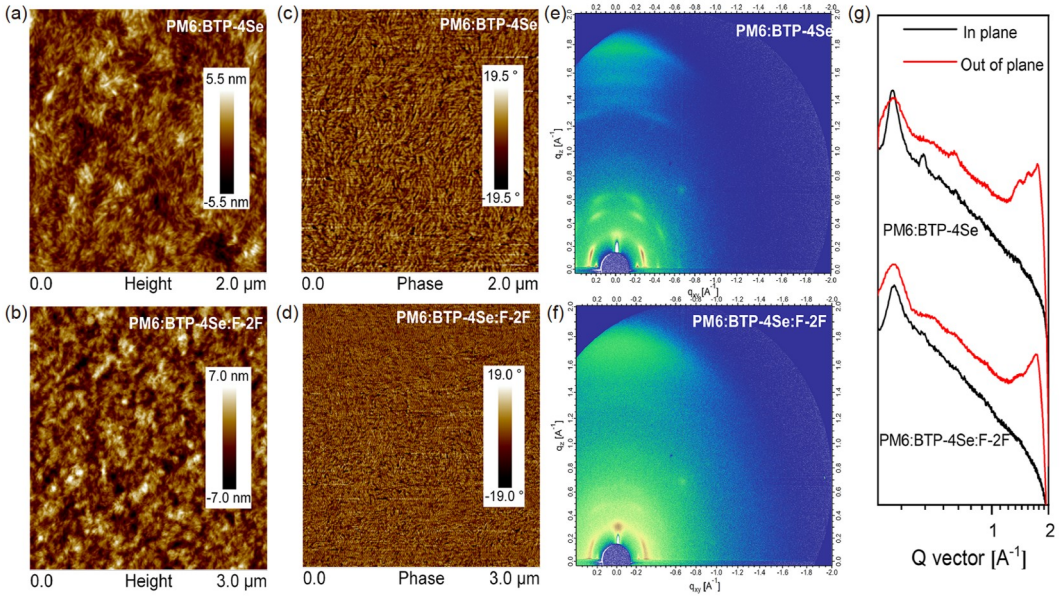

Figure 4 AFM height images of (a) PM6:BTP-4Se blend and (b) PM6:BTP-4Se:F-2F blend. AFM phase images of (c) PM6:BTP-4Se blend and (d) PM6:BTP-4Se:F-2F blend. 2D-GIWAXD diffraction images of (e) PM6:BTP-4Se blend and (f) PM6:BTP-4Se:F-2F blend. (g) 1D plots of the blend films in the in-plane and out-of-plane direction (color online).

showed smooth surface morphologies with the R_q values of 1.37 and 1.98 nm, respectively. In addition, as depicted in the AFM phase images in Figure 4c, d, clear interpenetrating structure with small fibers could be observed, indicating the similar degree of phase separation in the two blend films. The molecular packing ability was also investigated by the GIWAXS. As displayed in Figure S7, the pure film of the BTP-4Se presents a face-on orientation with a π-π stacking diffraction peak (010) around 1.65 Å in the OOP direction and lamellar packing diffraction peak (100) around 0.37 Å^{-1} in IP direction. After blending with the donor material PM6, as depicted in Figure 4e–g, the binary blend film shows an enhanced (010) peak at 1.74 Å^{-1}(d spacing: 3.60 Å) with a larger CCL value of 90.61 Å. However, after introducing the F-2F into the binary blend, the ternary blend exhibits a smaller CCL value of 33.84 Å and slightly larger π-π stacking distance of 3.72 Å, demonstrating that the addition of F-2F can slightly weaken the crystallinity of the binary blend and then avoid the possible over-aggregation and large phase separation [45], which is beneficial to charge transport and supporting the higher J_{sc} of the ternary device.

Besides the J_{sc}, the V_{oc} of the ternary device was also enhanced concurrently. The detailed E_{loss} analysis of the optimized binary and ternary devices were carried out according to the literature method [41]. As shown in Figure S8 and listed in Table S1, the ternary device showed a total lower E_{loss} with value of 0.489 eV than that of the binary device with the value of 0.509 eV, which comes from its lower ΔE_2 and ΔE_3. The optimal ternary device yields a higher EQE_{EL} of 1.96×10^{-4} than the binary device of 1.33×10^{-4}, corresponding to the calculated ΔE_3 of 0.221 V and 0.231 V, respectively. Besides, the ΔE_2 of the two systems could be obtained according to the above equation and are 0.029 and 0.019 V for the binary and ternary devices. The results indicate that the ternary strategy is an effective way to reduce the E_{loss} and get higher V_{oc}, which is more meaningful for constructing the series connected tandem OSCs.

2.3 Fabrication and photovoltaic performance of the tandem cells

The tandem devices with conventional structure were fabricated using the front and rear cells discussed above. An all solution-processed ICL composed of ZnO, PEDOT:PSS and phosphomolybdic acid hydrate (PMA) was used to connect the two subcells as shown in Figure 5a, where PMA worked as a hole transport layer to form an efficient ICL with PEDOT:PSS and ZnO as reported by Choy *et al.* [45]. The energy levels diagram of the tandem device was exhibited in Figure 5b. Before optimizing the performance of the tandem devices, the optical modeling conducting by the transfer matrix method was used to guide the thickness optimization of the subcells to obtain a high and balanced J_{sc}. The simulation results are exhibited in Figure 5c and the optimal J_{sc} of 13.49 mA cm^{-2} can be reached with the thickness value of 135 nm and 100 nm for the front and rear cell. Guided by the simulation results and after the device optimization, the tandem device achieved a best value of 19.55% with a V_{oc} of 1.880 V, a J_{sc} of 13.25 mA cm^{-2} and an excellent *FF* of 78.47%. The corresponding *J-V* curve was also shown in

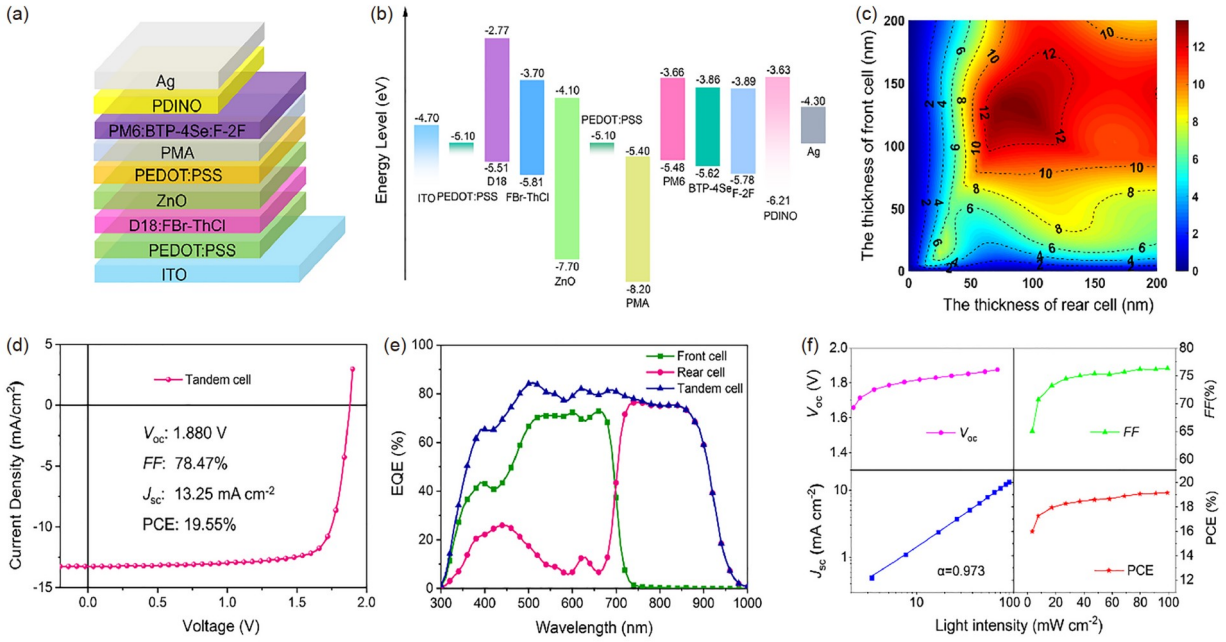

Figure 5 (a) Device architecture of the tandem device. (b) Energy level diagram of the tandem device. (c) Simulated current density generated in the tandem cell as a function of the thicknesses of the active layers. (d) *J-V* curve and (e) EQE of the optimal tandem device. (f) Variation of photovoltaic parameters of the tandem device under different light intensity (color online).

Figure 5d, and the detailed optimized photovoltaic parameters are summarized in Table 1.

To figure out the current match behavior of the subcells in tandem device, EQE measurement was carried out as shown in Figure 5e. The EQE response value of the front cell reaches over 70% in the range of 500–700 nm with an integrated J_{sc} of 13.11 mA cm^{-2}. The rear cell shows a broad EQE spectra to 1,000 nm with higher response values over 75% in 750–900 nm, and the integrated J_{sc} value is 13.44 mA cm^{-2}. The higher and well-balanced integrated J_{sc} is consistent with the values obtained from the *J-V* measurement and mainly ascribed to the complementary absorption range and optimal thickness, as well as the excellent photovoltaic performance of the front and real cells. Subsequently, the light intensity dependence of the tandem device performance was tested under different light intensity. As depicted in Figure 5f, there was a linear relationship between the J_{sc} and illumination intensities, indicating negligible space charge effects in the tandem device and interconnected layer [12,21].

3 Conclusions

In summary, we have designed and synthesized two acceptors named FBr-ThCl and BTP-4Se with complementary absorptions ranging from 300 to 1,000 nm for the fabrication of tandem OSCs under the guidance of the semi-empirical model we previously reported. The device based on D18:FBr-ThCl delivered a high V_{oc} of 1.053 V and a notable *FF* of 78.81%. Meanwhile, the ternary device of PM6:BTP-4Se:F-2F was optimized and delivered a PCE of 16.56% with a V_{oc} of 0.840 V, a J_{sc} of 26.88 mA cm^{-2}, and an *FF* of 73.36%, demonstrating the great potential as rear cell. Finally, the tandem cells were fabricated using an all solution processed ICL and demonstrated a high PCE of 19.55% with a V_{oc} of 1.880 V, a J_{sc} of 13.25 mA cm^{-2} and a notable *FF* of 78.47%. Our results highlight the great potential of tandem devices in boosting the performance of OSCs and demonstrate that the subcell materials design and device optimization are essential in pursuing high performance tandem OSCs. It is believed that PCE over 25% will be realized *via* the furtherly careful subcell materials design and device optimization.

Acknowledgements This work was supported by the National Natural Science Foundation of China (52025033, 21935007), the Ministry of Science and Technology of China (2022YFB4200400, 2019YFA0705900), the Tianjin City (20JCZDJC00740) and 111 Project (B12015).

Conflict of interest The authors declare no conflict of interest.

Supporting information The supporting information is available online at chem.scichina.com and link.springer.com/journal/11426. The supporting materials are published as submitted, without typesetting or editing. The responsibility for scientific accuracy and content remains entirely with the authors.

1 Park S, Heo SW, Lee W, Inoue D, Jiang Z, Yu K, Jinno H, Hashizume D, Sekino M, Yokota T, Fukuda K, Tajima K, Someya T. *Nature*, 2018, 561: 516–521

2 Sun Y, Chang M, Meng L, Wan X, Gao H, Zhang Y, Zhao K, Sun Z, Li C, Liu S, Wang H, Liang J, Chen Y. *Nat Electron*, 2019, 2: 513–520
3 Sun Y, Liu T, Kan Y, Gao K, Tang B, Li Y. *Small Sci*, 2021, 1: 2100001
4 Wadsworth A, Moser M, Marks A, Little MS, Gasparini N, Brabec CJ, Baran D, McCulloch I. *Chem Soc Rev*, 2019, 48: 1596–1625
5 Hou J, Inganäs O, Friend RH, Gao F. *Nat Mater*, 2018, 17: 119–128
6 Yu R, Wei X, Wu G, Zhang T, Gong Y, Zhao B, Hou J, Yang C, Tan Z. *Energy Environ Sci*, 2022, 15: 822–829
7 Chong K, Xu X, Meng H, Xue J, Yu L, Ma W, Peng Q. *Adv Mater*, 2022, 34: 2109516
8 Sun R, Wu Y, Yang X, Gao Y, Chen Z, Li K, Qiao J, Wang T, Guo J, Liu C, Hao X, Zhu H, Min J. *Adv Mater*, 2022, 34: 2110147
9 He C, Pan Y, Ouyang Y, Shen Q, Gao Y, Yan K, Fang J, Chen Y, Ma CQ, Min J, Zhang C, Zuo L, Chen H. *Energy Environ Sci*, 2022, 15: 2537–2544
10 Liu Y, Liu B, Ma CQ, Huang F, Feng G, Chen H, Hou J, Yan L, Wei Q, Luo Q, Bao Q, Ma W, Liu W, Li W, Wan X, Hu X, Han Y, Li Y, Zhou Y, Zou Y, Chen Y, Li Y, Chen Y, Tang Z, Hu Z, Zhang ZG, Bo Z. *Sci China Chem*, 2021, 65: 224–268
11 Liu Y, Liu B, Ma CQ, Huang F, Feng G, Chen H, Hou J, Yan L, Wei Q, Luo Q, Bao Q, Ma W, Liu W, Li W, Wan X, Hu X, Han Y, Li Y, Zhou Y, Zou Y, Chen Y, Liu Y, Meng L, Li Y, Chen Y, Tang Z, Hu Z, Zhang ZG, Bo Z. *Sci China Chem*, 2022, 65: 1457–1497
12 Meng L, Zhang Y, Wan X, Li C, Zhang X, Wang Y, Ke X, Xiao Z, Ding L, Xia R, Yip HL, Cao Y, Chen Y. *Science*, 2018, 361: 1094–1098
13 Cheng P, Li G, Zhan X, Yang Y. *Nat Photon*, 2018, 12: 131–142
14 Zuo L, Shi X, Jo SB, Liu Y, Lin F, Jen AKY. *Adv Mater*, 2018, 30: 1706816
15 Wang J, Zhang M, Lin J, Zheng Z, Zhu L, Bi P, Liang H, Guo X, Wu J, Wang Y, Yu L, Li J, Lv J, Liu X, Liu F, Hou J, Li Y. *Energy Environ Sci*, 2022, 15: 1585–1593
16 Zhou Y, Fuentes-Hernandez C, Shim JW, Khan TM, Kippelen B. *Energy Environ Sci*, 2012, 5: 9827
17 Ameri T, Li N, Brabec CJ. *Energy Environ Sci*, 2013, 6: 2390
18 Tavakoli MM, Si H, Kong J. *Energy Technol*, 2021, 9: 2000751
19 Liu G, Xia R, Huang Q, Zhang K, Hu Z, Jia T, Liu X, Yip H, Huang F. *Adv Funct Mater*, 2021, 31: 2103283
20 Jia Z, Qin S, Meng L, Ma Q, Angunawela I, Zhang J, Li X, He Y, Lai W, Li N, Ade H, Brabec CJ, Li Y. *Nat Commun*, 2021, 12: 178
21 Kim JY, Lee K, Coates NE, Moses D, Nguyen TQ, Dante M, Heeger AJ. *Science*, 2007, 317: 222–225
22 Dou L, You J, Yang J, Chen CC, He Y, Murase S, Moriarty T, Emery K, Li G, Yang Y. *Nat Photon*, 2012, 6: 180–185
23 You J, Dou L, Yoshimura K, Kato T, Ohya K, Moriarty T, Emery K, Chen CC, Gao J, Li G, Yang Y. *Nat Commun*, 2013, 4: 1446
24 Cheng P, Liu Y, Chang SY, Li T, Sun P, Wang R, Cheng HW, Huang T, Meng L, Nuryyeva S, Zhu C, Wei KH, Sun B, Zhan X, Yang Y. *Joule*, 2019, 3: 432–442
25 Meng L, Yi YQQ, Wan X, Zhang Y, Ke X, Kan B, Wang Y, Xia R, Yip HL, Li C, Chen Y. *Adv Mater*, 2019, 31: 1804723
26 Chen S, Zhang G, Liu J, Yao H, Zhang J, Ma T, Li Z, Yan H. *Adv Mater*, 2017, 29: 1604231
27 Lu S, Ouyang D, Choy WCH. *Sci China Chem*, 2017, 60: 460–471
28 Li M, Gao K, Wan X, Zhang Q, Kan B, Xia R, Liu F, Yang X, Feng H, Ni W, Wang Y, Peng J, Zhang H, Liang Z, Yip HL, Peng X, Cao Y, Chen Y. *Nat Photon*, 2016, 11: 85–90
29 Yuan J, Zhang Y, Zhou L, Zhang G, Yip HL, Lau TK, Lu X, Zhu C, Peng H, Johnson PA, Leclerc M, Cao Y, Ulanski J, Li Y, Zou Y. *Joule*, 2019, 3: 1140–1151
30 Zhu L, Zhang M, Xu J, Li C, Yan J, Zhou G, Zhong W, Hao T, Song J, Xue X, Zhou Z, Zeng R, Zhu H, Chen CC, MacKenzie RCI, Zou Y, Nelson J, Zhang Y, Sun Y, Liu F. *Nat Mater*, 2022, 21: 656–663
31 Chen H, Zou Y, Liang H, He T, Xu X, Zhang Y, Ma Z, Wang J, Zhang M, Li Q, Li C, Long G, Wan X, Yao Z, Chen Y. *Sci China Chem*, 2022, 65: 1362–1373
32 Wan X, Li C, Zhang M, Chen Y. *Chem Soc Rev*, 2020, 49: 2828–2842
33 Sun Y, Gao HH, Wu S, Meng L, Wan X, Li M, Ma Z, Guo Z, Li S, Zhang H, Li C, Chen Y. *Sci China Chem*, 2021, 64: 608–615
34 Huang Y, Meng L, Liang H, Li M, Chen H, Jiang C, Zhang K, Huang F, Yao Z, Li C, Wan X, Chen Y. *J Mater Chem A*, 2022, 10: 11238–11245
35 Zheng Z, Wang J, Bi P, Ren J, Wang Y, Yang Y, Liu X, Zhang S, Hou J. *Joule*, 2022, 6: 171–184
36 Wang J, Zheng Z, Zu Y, Wang Y, Liu X, Zhang S, Zhang M, Hou J. *Adv Mater*, 2021, 33: 2102787
37 Liu S, Yuan J, Deng W, Luo M, Xie Y, Liang Q, Zou Y, He Z, Wu H, Cao Y. *Nat Photon*, 2020, 14: 300–305
38 Li S, Li CZ, Shi M, Chen H. *ACS Energy Lett*, 2020, 5: 1554–1567
39 Liu W, Xu X, Yuan J, Leclerc M, Zou Y, Li Y. *ACS Energy Lett*, 2021, 6: 598–608
40 Liu Q, Jiang Y, Jin K, Qin J, Xu J, Li W, Xiong J, Liu J, Xiao Z, Sun K, Yang S, Zhang X, Ding L. *Sci Bull*, 2020, 65: 272–275
41 Shockley W, Queisser HJ. *J Appl Phys*, 1961, 32: 510–519
42 Liu H, Li M, Wu H, Wang J, Ma Z, Tang Z. *J Mater Chem A*, 2021, 9: 19770–19777
43 Chen XK, Qian D, Wang Y, Kirchartz T, Tress W, Yao H, Yuan J, Hülsbeck M, Zhang M, Zou Y, Sun Y, Li Y, Hou J, Inganäs O, Coropceanu V, Bredas JL, Gao F. *Nat Energy*, 2021, 6: 799–806
44 Yan C, Liu T, Chen Y, Ma R, Tang H, Li G, Li T, Xiao Y, Yang T, Lu X, Zhan X, Yan H, Li G, Tang B. *Sol RRL*, 2019, 4: 1900377
45 Lu S, Lin H, Zhang S, Hou J, Choy WCH. *Adv Energy Mater*, 2017, 7: 1701164